



Sedimentary and crustal structure of the US Gulf Coast revealed by Rayleigh wave and teleseismic P coda data with implications for continent rifting

Wenpei Miao^a, Fenglin Niu^{a,*}, Guoliang Li^{a,b}, Alan Levander^a

^a Department of Earth, Environmental and Planetary Sciences, Rice University, Houston, TX, USA

^b State Key Laboratory of Petroleum Resources and Prospecting, and Unconventional Natural Gas Institute, China University of Petroleum–Beijing, Beijing, China

ARTICLE INFO

Article history:

Received 25 July 2020

Received in revised form 16 October 2021

Accepted 19 October 2021

Available online xxxx

Editor: H. Thybo

Keywords:

Rayleigh waves

Joint inversion

US Gulf Coastal Plain

Continental rifting

Mississippi Embayment

ABSTRACT

We have developed an S-wave model of the south-central US focusing on the Gulf Coast sedimentary basin and its crust to understand continental rifting and regional tectonics. The model was derived by a joint inversion of Rayleigh wave phase velocities, Z/H ratios and P-coda data. The surface- and body-wave measurements were made, respectively, from ambient noise and teleseismic earthquakes recorded by 215 USArray stations in a rectangular area of 100° – 87° west and 28° – 37° north. We employed a cross-convolution function and H- κ analysis to better constrain sedimentary and Moho structure. We find that the southern edge of the Ouachita fold-and-thrust belt (OFTB) appears as a boundary in measured phase velocities, Z/H ratios, sediment basement depths, Moho depths, average crustal V_s and V_p/V_s ratios. The model shows southeastward thickening of the sedimentary basin, accompanied by thinning of the crystalline crust. The Moho gradient suggests that early rifting between North America and the Yucatan block commenced in a SE direction and involved most of the Pangea crust south of the OFTB boundary (i.e., Gondwana crust). We believe that a high velocity feature in the lowermost crust and upper mantle parallel to the southeast Texas coast was emplaced as a mafic body and is the source of the Houston magnetic anomaly. The seismic structures of the crust and uppermost mantle observed beneath the Mississippi Embayment and the Mississippi Valley Graben are consistent with plume induced Cretaceous uplift of the Mississippi Embayment as North America passed over the Bermuda hotspot.

© 2021 Elsevier B.V. All rights reserved.

1. Introduction

The Gulf of Mexico (GOM) ocean basin and the surrounding rifted margins have a number of notable features: They are almost entirely enclosed by the North American continent and Cuba. The northern edge of the rifted continental margin is a Paleozoic collisional orogeny, the Ouachita Fold and Thrust belt (OFTB). Continental rifting preceded seafloor spreading by ~ 40 Myrs, during which widespread salt deposits formed in shallow seas fed by Pacific sources. Although seafloor spreading lasted only ~ 20 Myrs, the direction of spreading rotated almost 90° . Owing to thick sediments that mask the stratigraphic record and basement, the style of rifting that created the US Gulf Coastal Plain (GCP) and led to the opening of the GOM is unclear (e.g., Marton and Buffler, 1993; Bird et al., 2005; Mickus et al., 2009; Stern and Dickinson, 2010; Van Avendonk et al., 2015; Nguyen and Mann, 2016). Models for

extension of the GCP can be grouped into two broad categories: 1) Pre-rift continental extension and seafloor spreading both occurred about a pole of rotation in the western Florida Strait (Dunbar and Sawyer, 1987; Hall and Najmuddin, 1994; Bird et al., 2005), and 2) The continent first extended to the southeast as the Gondwana Yucatan block moved away from North America, prior to seafloor spreading about the Florida Strait pole (Pindell and Dewey, 1982; Marton and Buffler, 1994; Hudec et al., 2013). Although usually associated with Pangea breakup and opening of the Atlantic, another model suggests that the entire GOM system is a back arc basin of a subduction zone along southwestern North America (Stern and Dickinson, 2010), and is only weakly related to or is coincidental with Atlantic opening.

Marton and Buffler (1993) proposed a lithospheric simple-shear model for the rifting and opening of the GOM based on the asymmetrical sediment and crustal distribution between the proximal northern margin and the distal southern (Yucatan) margin. The Texas and Louisiana Gulf coast margin has been interpreted as a magmatic rifted margin based on the Houston Magnetic anomaly which parallels the Texas coast (Mickus et al., 2009) and middle-

* Corresponding author.

E-mail address: niu@rice.edu (F. Niu).

late Jurassic alkaline igneous rocks entrained in coastal Louisiana salt diapirs (Stern et al., 2011). In contrast, Van Avendonk et al. (2015) found that seismic velocities in the crust under the Texas shelf are in the range of 5.0–7.0 km/s, too low to be consistent with an Atlantic style margin magmatic crust. They suggest that rifting of the northwestern GOM was unlikely magma assisted, and instead was due to passive response to far-field lithospheric stresses associated with the opening of the Atlantic. Seismic velocities in the continental margin crust are much higher further east, indicative of magma-assisted rifting (Christeson et al., 2014; Eddy et al., 2014).

The GCP is the onshore element of the extended passive margin lying between the OFTB and the Gulf of Mexico ocean basin (Fig. 1). The OFTB formed in the Carboniferous during assembly of the supercontinent Pangea. The extended continental margin formed in late Triassic–Early Jurassic (~200–160 Ma) during the breakup of Pangea (Pindell and Dewey, 1982; Harry and Londono, 2004). Significant tectonic features surrounding the GCP and OFTB include 1) the OFTB's foreland basins, the Fort Worth, Arkoma, and Black Warrior basins, 2) the Precambrian Southern Oklahoma Aulacogen (SOA), and 3) the Cretaceous Mississippi Embayment (ME) overlying the Precambrian Mississippi Valley Graben (MVG).

The SOA is the southeastern end of the Wichita mega-shear (Budnik, 1986), part of a rift system associated with the Permian formation of the Ancestral Rocky Mountains and was further deformed during the Ouachita orogeny. The MVG located in the northern ME region (Fig. 1), is a ~70-km-wide depression formed by rifting in late Precambrian or early Paleozoic time. Hildenbrand (1985) found an anomalously dense layer at the base of the crust underneath the seismically active part of the graben and suggested that the anomaly likely facilitated strain accumulation, resulting in the occurrence of the earthquakes of the New Madrid Seismic Zone. In contrast, the ME is a broad, shallow southwest plunging basin that extends from southeastern Missouri and southwestern Kentucky into the northern GCP and is filled with ~1.5 km of Cretaceous and Cenozoic sediments (Cox and Van Arsdale, 2002). Although originally thought to have been caused by extension during the late opening of the GOM (Braile et al., 1986), Cox and Van Arsdale (2002) noted that it formed ~60 Myrs after cessation of GOM seafloor spreading, and instead proposed that the MVG was uplifted 1–3 km in the Cretaceous and early Cenozoic when North America passed over the Bermuda plume. The uplifted graben eroded, and once the MVG moved off the plume, it subsided to create a topographic low, allowing for the infill of fluvio-marine sediments.

The USArray project was designed to image the Earth's lithosphere and mantle beneath the US to understand continental tectonics, lithosphere deformation and to assess earthquake hazard. There was a total of ~2200 temporary deployments of broadband seismometers with a station spacing of ~70 km across the US (Meltzer et al., 1999). The crust and upper mantle beneath the GCP and its surrounding areas have been studied by various seismic imaging techniques using USArray data, such as traveltime tomography (Evanzia et al., 2014), surface wave tomography (Yao and Li, 2016), receiver function (RF) analysis (Ainsworth et al., 2014), joint analysis of surface wave dispersion and P-wave receiver function data (Agrawal et al., 2015). Shen and Ritzwoller (2016) jointly inverted Rayleigh wave dispersion, Rayleigh wave ellipticity and 10-s long RF data recorded by the USArray and constructed an S-wave velocity model of the contiguous US with a spatial sampling of $0.25^\circ \times 0.25^\circ$.

In this study, we develop a regional three-dimensional (3-D) S-wave velocity (V_s) model of the sedimentary and crustal structure beneath the GCP and its surrounding areas to better constrain different models proposed for GCP rifting, GOM opening, and ME formation. Since Rayleigh wave dispersion is sensitive to vertically

integrated V_s , and receiver side teleseismic P_s conversions are sensitive to the vertical derivative of V_s , these two datasets complement each other to better constrain V_s . Neither Rayleigh wave dispersion nor deconvolution-based RF analyses, however, are effective at resolving shallow sedimentary structures. Previous studies have shown that Rayleigh-wave ellipticity or Z/H ratio is more sensitive to shallow structure than phase velocity dispersion data of the same period (e.g., Lin et al., 2012, 2014; Chong et al., 2014), allowing a better constraint on near-surface V_s structure by using Z/H ratio data. Joint inversion of the three datasets (Rayleigh wave phase velocities, Z/H ratios, and RFs) better constrains shallow V_s structures (Shen and Ritzwoller, 2016). This type of joint inversion can be degraded by poor quality RFs made with data from stations located on unconsolidated sediments due to strong sediment reverberations that obscure the Moho P-to-S conversion. Li et al. (2019) replaced deconvolution-based RFs with cross-convolution functions as the misfit function of body wave data in the joint inversion of surface and body wave data. Cross convolution effectively takes sediment reverberations into account, therefore better constraining both the absolute velocities and their gradients in the shallow depths.

The current joint inversion model (Shen and Ritzwoller, 2016) used the first ~10 s P-wave coda for the RFs, omitting the crustal reverberation phases that constrain Moho depth. This can lead to large errors in crustal thickness estimates due to the tradeoff between V_p/V_s ratio (κ) and crustal thickness (H). In this study we first applied H- κ analysis to individual RFs to obtain crustal thickness and average crustal V_p/V_s ratio. We used the H- κ results for the starting Moho model in the joint inversion with Moho depth allowed to vary within $H \pm 4$ km. Finally, we applied the joint inversion method of Li et al. (2019) using surface and body wave data to obtain a 3-D V_s model to a depth of 70 km.

2. Data and methods

We selected 215 USArray Transportable Array (TA) stations located in a rectangular area from $100^\circ \sim 87^\circ\text{W}$ and $28^\circ \sim 37^\circ\text{N}$ lying in the south-central United States (Fig. 1a). The TA stations recorded 19–24 months of data between 02/2009 and 12/2013. We computed RFs from teleseismic events and Rayleigh wave Green's functions from the continuous ambient noise data. We employed a Markov Chain Monte Carlo method to jointly invert phase velocities, Z/H ratios and cross-convolution functions derived from these data to obtain a 3-D S-wave velocity model of the crust and upper mantle beneath the study area.

2.1. Receiver functions and H- κ analysis

We manually selected 3-component (3-C) waveforms from a total of 365 earthquakes with magnitudes greater than 5.6 in the epicentral distance range of 30° and 90° (Fig. 1c). We first rotated the two horizontal components into radial and transverse directions. We then computed the principal directions (longitudinal and in-plane transverse) of the 2-D covariance matrix calculated from the vertical and radial directions, and further projected the vertical and radial components into the two principal directions, which are hereafter referred to as P- and SV-components (Niu et al., 2007). We applied the “water-level” deconvolution technique (Clayton and Wiggins, 1976) to the P- and SV-components to generate RFs. We manually checked all RFs, selecting good quality ones for further analysis, giving a total of 5 to 209 RFs per station. We employed a refined H- κ stacking method (Niu et al., 2007), which introduced a cross-correlation-based weighting function in summing the Moho P_s conversion and the two multiples. We used the weights 0.5, 0.25, and 0.25 for the three phases in a grid search to find the

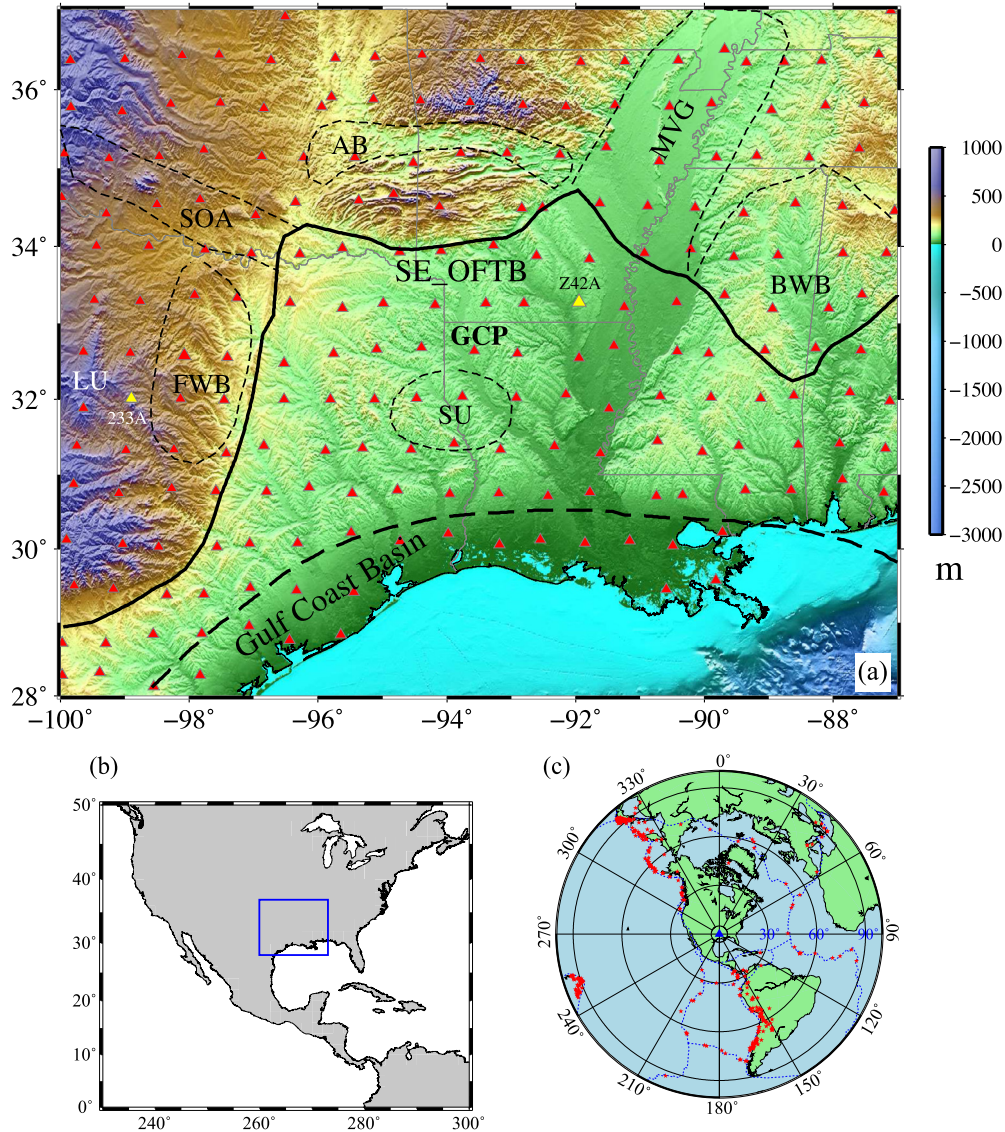


Fig. 1. (a) Topographic map showing the Gulf Coastal Plain (GCP) and its surrounding areas. Red triangles represent the 215 USArray stations used in this study. The two yellow triangles indicate the locations of the two stations shown in Figs. 3–5. The solid black line indicates the Ouachita fold-and-thrust belt (OFTB). The dashed black lines indicate the Gulf Coast Basin (GCB), the Black Warrior Basin (BWB), Mississippi Valley Graben (MVG), Arkoma Basin (AB), Southern Oklahoma Aulacogen (SOA), Fort Worth Basin (FWB), and Sabine uplift (SU). LU is the Llano Uplift. (b) Map of Americas showing the study area (rectangle). (c) Location of the 365 earthquakes (solid stars) used in receiver function analysis. The solid triangle at the center of the circles indicates the center of the study area, roughly located at 32.5° N and 93.5° W. Note that although some events fall into the 30° circle and out of the 90° circle from the center, we only selected stations with an epicenter distance between 30° and 90°. (For interpretation of the colors in the figure(s), the reader is referred to the web version of this article.)

(H, κ) pair that yields the greatest summed amplitude. Two examples of the H - κ stacking results at station 233A and Z42A are shown in Figure S1.

2.2. Computing cross-correlation tensor from ambient noise data

For the ambient noise tomography, following Lin et al. (2014) we first collected 3-C continuous records from the 215 USArray stations over their entire deployment period. We cut the continuous data into daily epochs, removed instrument responses, linear trends and means, bandpass filtered the records from 0.02 to 0.4 Hz and downsampled the data to 1 Hz. We applied a temporal normalization using a running-absolute-mean normalization method and spectral whitening to all the three components at each station to retain their relative amplitudes. After preprocessing we calculated the cross-correlation functions (CCFs) between all the three components for all station pairs. For each station pair, we had nine CCFs, which were ZZ, ZE, ZN, EE, EN, EZ, NN, NE, and NZ,

respectively. These 9 CCFs formed a 3 by 3 tensor known as the cross-correlation tensor (CCT).

2.3. Estimating Rayleigh wave Z/H ratio

During preprocessing we applied the same temporal normalization and spectral whitening to all the 3-C records of each station, thus preserving relative amplitudes. To measure Rayleigh wave Z/H ratios, we linearly stacked the daily CCTs of each station pair, then rotated the nine components to obtain, ZZ, ZR, RZ, and RR CCFs using the rotation matrix defined in Li et al. (2016). We kept the causal parts of the CCT for Z/H ratio measurement, since the causal parts relate to the Green's function traveling from the source station to the receiver station, and the Z/H ratio is mainly controlled by the structure beneath the receiver station (Tanimoto and Rivera, 2008).

For the station pair A-B, the Z/H ratio for a given period at station B can be estimated from:

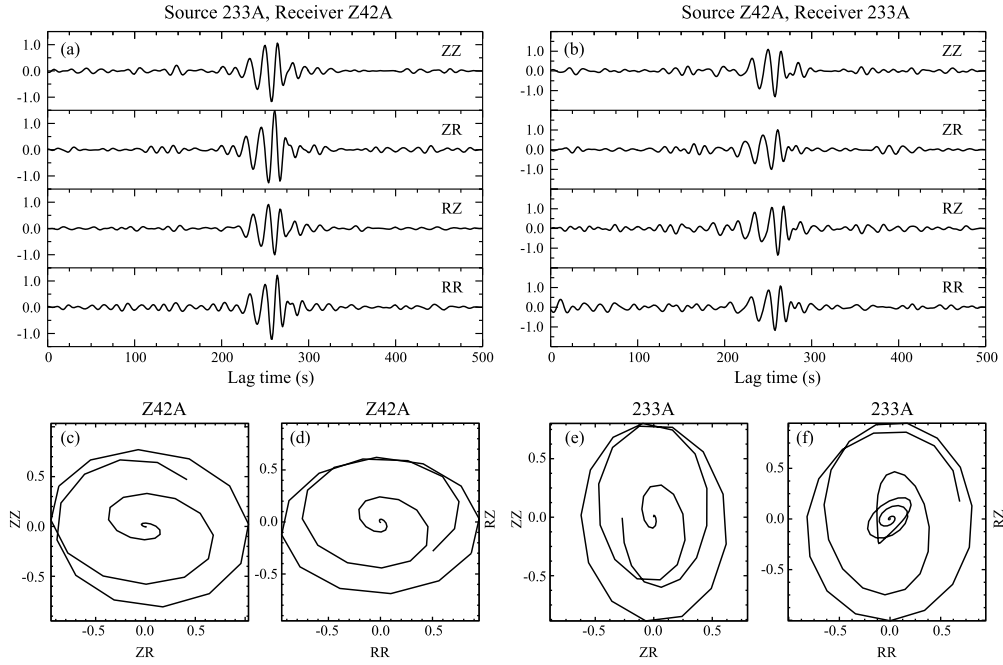


Fig. 2. Examples of the calculated ambient noise Green's functions between station pair 233A and Z42A. Locations of the two stations are shown in Fig. 1a. (a) 233A as the source station and Z42A as the receiver station. (b) vice versa. (c) and (d) Rayleigh wave particle motions at the Z42A, excited by a vertical (c) and a radial (d) source, respectively. (e) and (f) are same as (c) and (d) except for 233A. Note the low Z/H ratio at Z42A and high Z/H ratio at 233A, which are located inside the GCP and LU, respectively.

$$ZH_B(T) = \frac{Z_A Z_B}{Z_A R_B} = \frac{R_A Z_B}{R_A R_B} = \frac{Z_B Z_A}{R_B Z_A} = \frac{Z_B R_A}{R_B R_A} = \frac{Z_{stack}}{R_{stack}}, \quad (1)$$

where

$$\begin{aligned} Z_{stack} &= Z_A Z_B + iH[R_A Z_B] + Z_B R_A + H[Z_B R_A] \\ R_{stack} &= H[Z_A R_B] + R_A R_B + iH[R_B Z_A] + R_B R_A \end{aligned} \quad (2)$$

Here the first letter indicates the virtual source force direction, and the second letter represents the seismogram component, with Z and R being the vertical and radial directions. For example, $Z_A R_B$ represents the Green's function recorded on the radial component of station B from a vertical impulse source at station A. $H[\]$ in equation (2) denotes Hilbert transformation used to correct the 90° phase difference between different Rayleigh wave Green's functions components. After phase correction the four CCFs of each component are in-phase and are stacked to increase the signal-to-noise ratio (SNR) of the two components, i.e., Z_{stack} and R_{stack} . The stacked vertical and radial component Rayleigh waves were then narrow-band pass filtered in bands between 8–25 s to compute Z/H ratios at different periods. For each set of filtered Z_{stack} and R_{stack} , we calculated their zero-lag cross-correlation coefficient, and discarded pairs with a coefficient less than 0.8. The Z/H ratio is estimated from the maximum amplitude of the envelope functions of the filtered Z_{stack} and R_{stack} . For each station, we computed the Z/H ratios of all possible station pairs with their average as the final estimate of the Z/H ratio at the station.

An example of calculated ZZ, ZR, RZ, and RR CCFs between the station pair 233A and Z42A is shown in Fig. 2. Z42A inside the GCP has the horizontally elongated elliptical particle motion expected for a deep sedimentary basin (Figs. 2c and 2d), while 233A at the Llano Uplift shows the vertically elongated elliptical particle motion expected for a crystalline upper crust (Figs. 2e and 2f).

2.4. Rayleigh wave phase velocity measurement

We extracted Rayleigh wave phase velocity dispersion curves from ZZ CCFs. To improve SNRs of the Rayleigh wave arrivals

we first sorted the daily CCFs in chronological order and linearly stacked them every five days to create 5-day stacks of CCFs. We then stacked these five-day CCFs using the time-frequency phase weight stacking (tf-PWS) method (Li et al., 2018), which is more effective in improving SNR than a linear stack. We also folded the CCFs around time zero and stacked the causal and acausal segments to create symmetrical CCFs. We computed the SNRs of the causal segment and acausal segment of the CCFs as well as the symmetrical CCFs and chose the one with the highest SNR for phase velocity measurement. We employed the automated frequency-time analysis (FTAN, Dziewonski et al., 1969) and phase matched filtering (Herrin and Goforth, 1977) to estimate phase velocities in the period range of 8 to 40 s. Among all the station pairs, we only selected CCFs with a SNR greater than 10 from pairs with an inter-station distance larger than two wavelengths. We inverted the measured phase velocities along all the station pairs for phase velocities on a 0.25×0.25 -degree grid of the study area. Checkerboard tests (Figure S2) indicate that there are enough crossing raypaths for the inversion to recover anomalies with a size of $0.25^\circ \times 0.25^\circ$.

2.5. Cross-convolution functions of teleseismic P-wave coda field

Although the strong sediment reverberations can significantly degrade RFs, the method can be modified to provide key information on sedimentary structures. Instead of using regular RFs, Li et al. (2019) introduced the cross-convolution misfit function in the surface-body-wave joint inversion, which was computed from two cross convolution functions of the vertical and radial components between observed seismograms and synthetic Green's functions of a trial model (Bodin et al., 2014). As the Green's functions of sediment response remain almost unchanged over epicentral distance of 30° to 90° , Li et al. (2019) used the stacked seismograms to compute the two cross-convolution functions to increase the efficiency of the joint inversion:

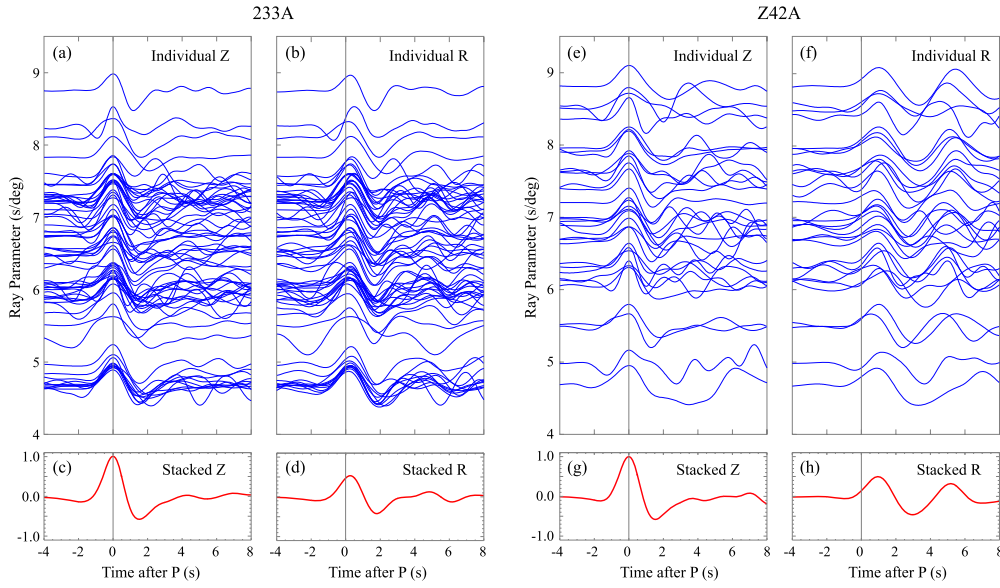


Fig. 3. Individual vertical- and radial-component waveforms of teleseismic events recorded at station 233A are plotted as a function of ray parameter in (a) and (b). The stacked vertical and radial components of waveforms are shown in (c) and (d), respectively. (e), (f), (g), and (h) are similar to (a), (b), (c), and (d), except for station Z42A. Note the large second pulse on the radial component of station Z42A, which is located inside the GCP.

$$h_{syn}(t, m) * \frac{1}{N} \sum_{i=1}^N V_{obs,i}(t) = h_{syn}(t, m) * v(t) * I(t) * \frac{1}{N} \sum_{i=1}^N s_i(t)$$

$$v_{syn}(t, m) * \frac{1}{N} \sum_{i=1}^N H_{obs,i}(t) = v_{syn}(t, m) * h(t) * I(t) * \frac{1}{N} \sum_{i=1}^N s_i(t)$$

(3)

Here $V_{obs,i}(t)$ and $H_{obs,i}(t)$ are the observed vertical and radial seismograms of the i^{th} event, while $v_{syn}(t, m)$ and $h_{syn}(t, m)$ are the synthetic vertical and radial Green's functions of a trial model m . N is the total number of teleseismic events. $I(t)$ and $s_i(t)$ represent the instrument response and the source time function of the i^{th} teleseismic event, respectively. $v(t)$ and $h(t)$ are the vertical and radial Green's functions of the earth. As the trial model, m , approaches the true earth, the two cross-convolution functions in equation (3) become identical.

We manually selected teleseismic events with a relatively simple source time functions and an SNR greater than 5. Most stations have more than 10 events. We first aligned all the seismograms to the peaks of the vertical records, and further normalized them by the peak amplitude of each vertical record. For those vertical records with negative peaks, we reversed the polarity of both the vertical and radial components before stacking. Finally, we stacked all the aligned normalized vertical and radial records, respectively, to create the vertical and radial records of a virtual teleseismic event. Fig. 3 illustrated two examples of the individual and stacked vertical and radial records at stations 233A and Z42A located on the LU and the GCP, respectively.

We then define the cross-convolution misfit function, $\chi(m)$, from the stacked vertical ($V_{stk}(t)$) and radial ($H_{stk}(t)$) records:

$$\chi(m) = 1 - \frac{\int_{T_1}^{T_2} \{V_{stk}(t) * h_{syn}(t, m)\} \cdot \{H_{stk}(t) * v_{syn}(t, m)\} dt}{\sqrt{\int_{T_1}^{T_2} |V_{stk}(t) * h_{syn}(t, m)|^2 dt} \cdot \sqrt{\int_{T_1}^{T_2} |H_{stk}(t) * v_{syn}(t, m)|^2 dt}} \quad (4)$$

Here, T_1 and T_2 define the time window of the direct P wave and sediment reverberations, which were set to 3 s before and 7 s after P.

2.6. Joint inversion

For each station we first constructed its phase velocity dispersion curve by a linear interpolation of values taken from its surrounding four grids. We then jointly inverted the phase velocities, Z/H ratios, and $\chi(m)$ calculated at each station to obtain a 1-D S-wave velocity model beneath the station using a Bayesian Monte Carlo approach. More specifically, we employed the Markov Chain Monte Carlo (MCMC) method (e.g., Afonso et al., 2013). The joint misfit function $M_{joint}(m)$ is defined by

$$M_{joint}(m) = M_c(m) + M_{ZH}(m) + M_{BW}(m)$$

$$= \frac{1}{N} \sum_{i=1}^N \frac{[C_i(m) - C_i^{obs}]^2}{\sigma_1^2} + \frac{1}{M} \sum_{j=1}^M \frac{[ZH_j(m) - ZH_j^{obs}]^2}{\sigma_2^2} + \frac{\chi(m)}{\sigma_3^2} \quad (5)$$

Here, C_i^{obs} and ZH_j^{obs} are the observed phase velocities and Z/H ratios, while $C_i(m)$ and $ZH_j(m)$ represent the calculated phase velocities and Z/H ratios at the i^{th} and j^{th} periods of a trial model generated by the Monte Carlo method. N and M are the numbers of periods of phase-velocity and Z/H ratio measurements, respectively. $\chi(m)$ is the cross-convolution misfit function defined in equation (4). Since uncertainties (σ_1 , σ_2 , and σ_3) of the three types of datasets are usually difficult to determine, we treated them as unknown parameters, which we also inverted for during the joint inversion. For a given model, we used the method from Computer Programs in Seismology (Herrmann and Ammon, 2004) to compute the Rayleigh wave phase velocities, Z/H ratios, and the Thomson-Haskell propagator matrix method (Haskell, 1962) to calculate synthetic Green's functions.

We divided the 1-D velocity model beneath each station into three layers, a sedimentary layer, a crystalline crust layer, and an upper mantle layer. We assumed V_s in the sedimentary layer increases linearly with depth, therefore V_s within the sediments can be determined by three parameters: V_s at the top, V_s at the bottom, and the layer thickness. The V_p/V_s ratio in the sediment was

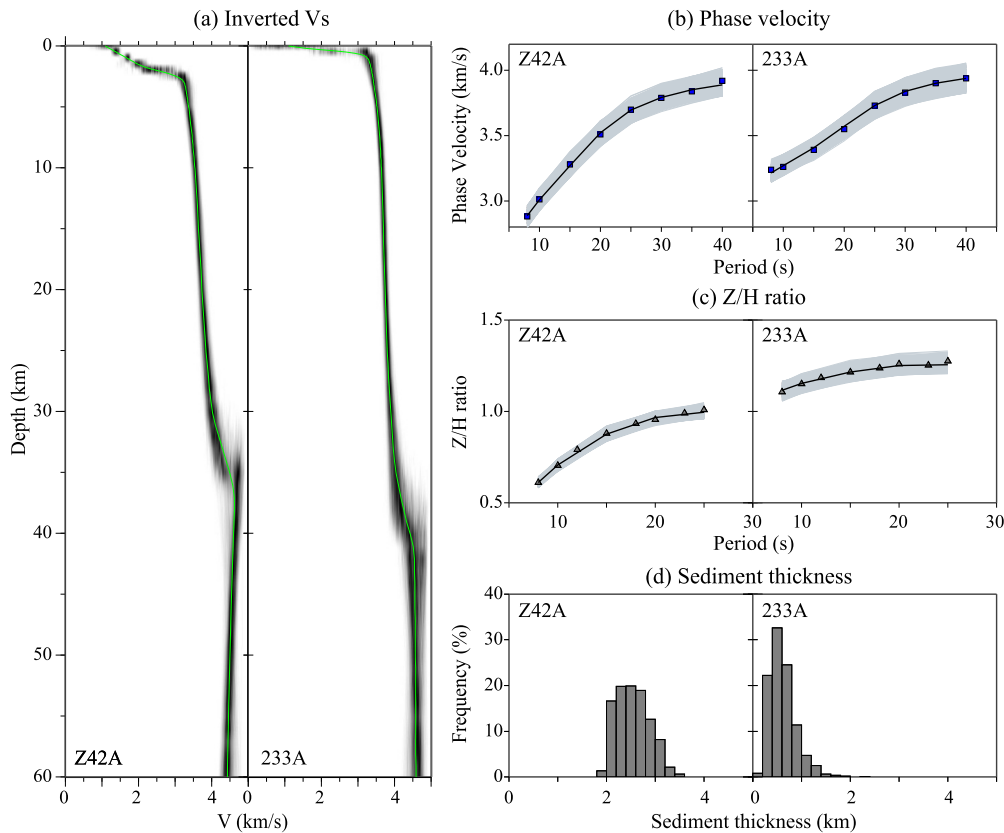


Fig. 4. Two examples of the joint inversion. (a) The inverted V_s models at Z42A (left) and 233A (right) are shown in green lines. The models are the averages of the 3000 V_s models with the lowest misfits, which are shown in thin grey lines. (b) The observed phase velocities at the two stations are shown together with predictions of the 3000 models (thin grey lines) and their averages (thick dark line). (c) Same as (b) except for Z/H ratio. (d) Histogram of sediment thickness estimated from 3000 models.

treated as a fourth parameter. We employed B-splines to represent V_s variations over depth in the crystalline crust and the upper mantle layers. In the crystalline crust, we used a total of five independent parameters including four B-spline coefficients and the Moho depth. In the mantle layer, we used four B-spline coefficients for V_s . Thus each 1-D model had a total of 13 independent parameters, which were perturbed in very wide depth and velocity ranges, except for the Moho depth. We didn't invert V_p/V_s ratio of the crystalline crust and the upper mantle because the phase velocity, Z/H ratio and cross-convolution data used in the inversion generally have poor resolution on P-wave velocity.

We set the V_p/V_s ratio to 1.75 in the crystalline crust, and 1.80 in the upper mantle. We used results of the $H-\kappa$ analysis of RF data as the initial Moho depth. In the inversion, Moho depths were allowed to vary ± 5 km relative to their initial values. Since the longest period of Rayleigh waves that we used in this study is 40 s, we only inverted for S-wave velocity structure from earth's surface to 70 km depth. We kept the PREM model (Dziewonski and Anderson, 1981) in the depth range of 70–200 km and used a constant V_s below 200 km.

For each station, we randomly generated 400,000 models and calculated the joint misfit function of equation (5). We then chose the best 3000 models with the lowest misfits to derive the final inversion results, i.e., we used the average and standard deviation of the 3000 models as the final 1-D model and the model uncertainty. In Fig. 4, we show two examples of the inverted 1-D velocity modes at stations 233A and Z42A. Station 233A is located north to the Precambrian Llano Uplift behind the OFTB while station Z42A is deployed inside the GCP (Fig. 1). The inverted V_s profile at Z42A shows a prominent low-velocity sediment layer in the top 5 km, which leads to the observed low Z/H ratios and phase velocities.

3. Results

3.1. $H-\kappa$ analysis

Among the 215 stations, we obtained robust measurements of crustal thickness and average crust V_p/V_s ratio from a total of 207 stations, listed in Table S1 and shown in Fig. 5a and Fig. 5b. We employed an inversion scheme to interpolate the 207 measurements onto a $0.25^\circ \times 0.25^\circ$ grid using a flatness constraint (Niu et al., 2007). Crustal thickness varies from 21.4 km to 48.9 km with an average of 35.8 km, while V_p/V_s ratio varies from 1.618 to 2.094 with an average of 1.857 across the study area. We find that the GCP has a relatively thin crust (Fig. 5a) and an elevated V_p/V_s ratio (Fig. 5b). The Ouachita Mountains also show a distinctly high V_p/V_s ratio.

3.2. Z/H ratios

To retain the most reliable Z/H ratio measurements, we required Rayleigh waves recorded on both the Z and R components with $\text{SNR} > 8$, and selected station pairs more than two wavelengths apart. The number of Z/H ratio measurements per station is greater than 20, with each following a Gaussian distribution with a standard deviation less than 0.12.

We obtained Z/H ratios from 204 stations. Fig. 6 shows the Z/H ratio maps at four different periods, 10 s, 15 s, 20 s and 25 s. At 10 s (Fig. 6a), the high and low Z/H regions are roughly divided by the southern edge of the OFTB (SE_OFTB, solid black line in Fig. 6). To the south the GCP has prominent low Z/H ratios that decrease steadily to the coast (Fig. 6). To the north Z/H ratios are high, including over the Llano Uplift and the Ouachita Mountains. The Z/H ratio at 10 s is mostly sensitive to velocity structure in

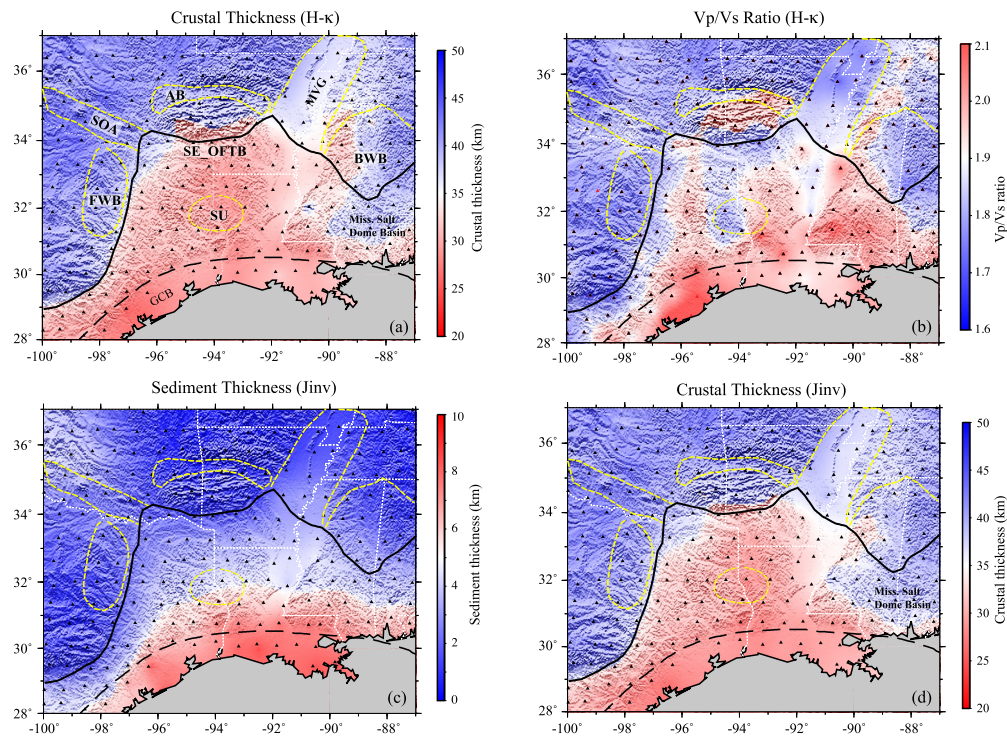


Fig. 5. Maps showing the crustal thickness (a) and V_p/V_s ratio (b) determined by $H-\kappa$ analysis of receiver function data. The color contour is based on the observations at stations shown as solid black triangles. Interpolation was performed to minimize the lateral variations of crustal thickness and V_p/V_s ratio (see text for details). Boundaries and tectonic units are similar to Fig. 1a. (c) Maps showing sediment (c) and crustal thickness (d) from the joint inversion. Scales of the color contours are shown on the right side of each map.

the top 5 km, and a low Z/H ratio is generally caused by low velocity sediments. The Paleozoic peripheral foreland basins north of the OFTB, such as the Fort Worth Basin and the Black Warrior Basin show a moderate Z/H ratio of 1.0–1.2, reflecting the Paleozoic sediments in the basins in contrast to the younger sediments in the GCP and Gulf Coast Basin (Fig. 6a). The early Paleozoic MVC in the northeast part of the study area possesses a low Z/H ratio, which is likely related to the recent Cretaceous and Cenozoic sediments. The Z/H ratio increases slightly with increasing period. At 25 s, the most prominent low Z/H ratio anomaly lies inside the Gulf Coast Basin.

3.3. Phase velocity maps

Fig. 7 shows four phase velocity maps at periods of 10 s, 15 s, 20 s, and 25 s. The measured phase velocity at 10 s exhibits a good spatial correlation with surface geology (Fig. 7a). High and low phase velocity regions are bordered by the southern edge of OFTB (black line in Fig. 7). South of the OFTB, negative phase velocity anomalies generally decrease with increasing period, with the largest anomalies appearing over the Gulf Coast, reflecting the increasing thickness of the sedimentary basins. The Sabine Uplift shows slightly higher phase velocities than the surrounding areas at 10 s and 15 s periods (Figs. 7a and 7b). Another low phase velocity band at all periods runs across the SOA in the NW of the study area (Fig. 7a).

3.4. 3-D Vs model

We jointly inverted Rayleigh wave phase velocities, Z/H ratio data, and cross-convolution misfit function data for a 1-D V_s model beneath each station following the joint inversion method described in section 2.6. We interpolated them onto a 0.25×0.25 -

degree grid of the study area using a minimum curvature surface-fitting method to construct the final 3-D V_s model.

The sedimentary thickness map is shown in Fig. 5c. The foreland basins of the OFTB, the Fort Worth, Arkoma, and Black Warrior Basins, are filled with similar amount of low-velocity sediments, ~ 1.5 km deep on average. South of the OFTB, the low-velocity sedimentary layer within the GCP is ~ 3 km thick and gradually deepens towards the coast, reaching almost 11 km depth in the Gulf Coast Basin. In the northwest and north, the sedimentary layer is ~ 4 km thick in the SOA and its neighbor, the Paleozoic Anadarko Basin. In the northeast low-velocity sedimentary infill inside the MVC is relatively thin, varying between ~ 1.0 km and ~ 2.3 km with an average of ~ 1.6 km.

The inverted crustal thickness (Fig. 5d) generally agrees well with the $H-\kappa$ results (Fig. 5a) and varies from ~ 25 + km in the coastal area to 40–45 km in the interior north of the OFTB belt (Fig. 5d). The crust beneath the GCP is relatively thin with an average of ~ 30.2 km except for the Mississippi Salt Dome Basin, where the crust is 35–42 km thick. The OFTB front (SE_OFTB, solid black line in Fig. 5d) is seen as a topographic boundary in the Moho, which decreases in depth by 5 to 10 kilometers crossing the boundary from the continental interior toward the coast. Crust beneath the Llano Uplift and the Fort Worth Basin in the western side of the OFTB is ~ 40 km thick and becomes slightly thicker (~ 42 km) beneath the SOA. On the other hand, the MVC and Black Warrior Basin on the northeast corner and east side of the study area have a slightly thin crust, ~ 36 km and ~ 38 km thick, respectively, very similar to that beneath the Ouachita Mountains and the Arkoma Basin (Fig. 6d).

Fig. 8 shows V_s maps at nine different depths. At 1 km depth, the GCP and the MVC are characterized by very low V_s , reflecting the young sediments in these areas. On the other hand, S-wave velocities inside the Paleozoic foreland Fort Worth, Arkoma, and Black Warrior Basins north of the OFTB are relatively high.

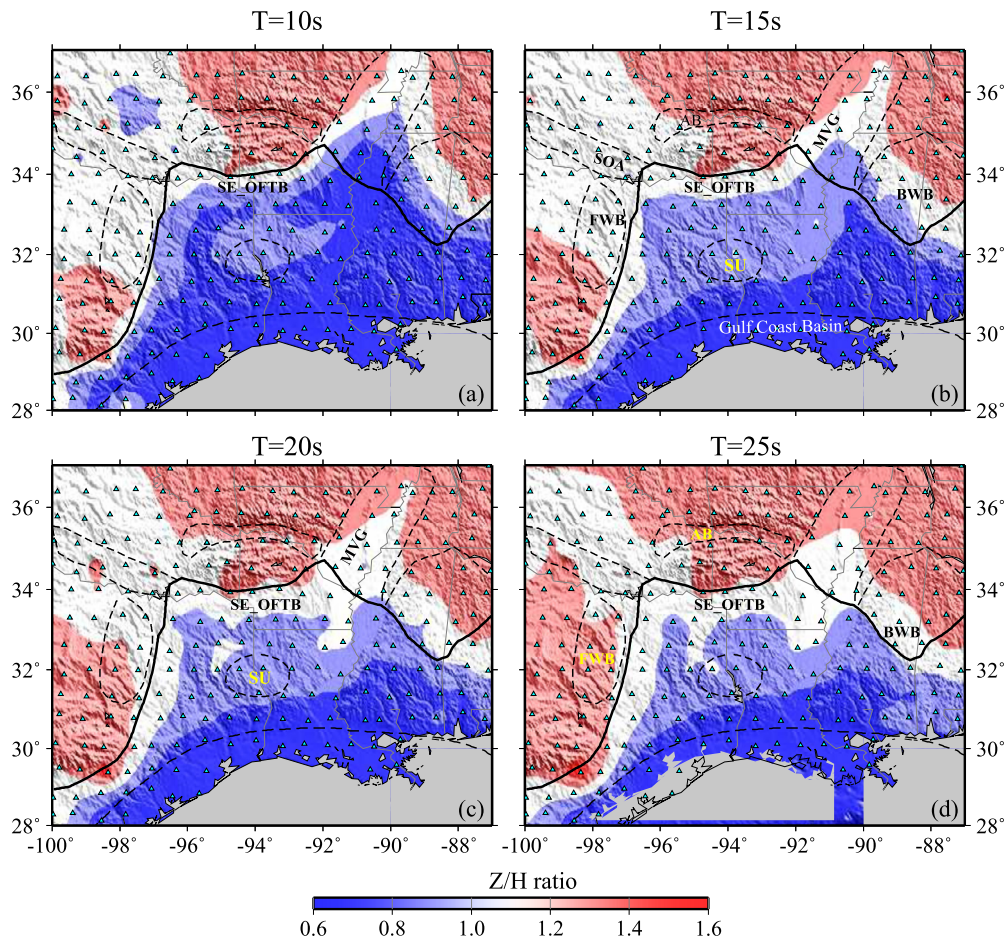


Fig. 6. Maps showing Rayleigh wave Z/H ratios of four different periods, 10 s (a), 15 s (b), 20 s (c) and 25 s (d) measured from ambient noise data. Boundaries and tectonic units are similar to Fig. 1a. Note that SE_OFTB marks the boundary between the low Z/H area and high Z/H ratio regions, especially for the two short periods.

The SOA and the Anadarko Basin in the northwestern part of the study area also feature low V_s . At 3 km depth (Fig. 8b) the low-velocity anomaly persists beneath the GCP, SOA and Ouachita Mountains, but disappears beneath the northeastern MVC. This evolving trend further continues at 5 km depth (Fig. 8c). The low-velocity anomaly vanishes completely beneath the MVC, but remains beneath the SOA, Ouachita Mountains, and large parts of the GCP.

At 8 to 23 km depth, we observe relatively low V_s beneath the SOA, Ouachita Mountains, and a large part of the GCP (Figs. 8d–8f). At 23 km depth (Fig. 8f) we observe a high V_s beneath the Gulf Coast Basin along the coast, where mantle is reached at this depth, consistent with the crustal thickness map shown in Fig. 5d. At 33 km depth (Fig. 8g) most of the GCP is mantle, showing a reversed velocity contrast between it and the surrounding areas, which are upper mantle and lower crustal velocities, respectively. In particular, the southeast Texas Gulf Coast Basin has a very high V_s , ~ 4.7 km/s, that extends to 40 km and 50 km depth (Figs. 8h and 8i). This is close to the S-wave speed of cratonic lithosphere (e.g., Grand, 1994), which is attributed to both low temperature and composition of the cratonic keel (Lee, 2003). This high-velocity anomaly is spatially correlated with the so-called Houston magnetic anomaly, a narrow high magnetic intensity band along the southeast Texas coast (Mickus et al., 2009). The uppermost mantle beneath the GCP shows a moderate V_s of ~ 4.5 km/s, except for the Mississippi Salt Dome Basin, which has a V_s of ~ 4.6 km/s, slightly higher than the global average (~ 4.5 km/s). On the other hand, the uppermost mantle beneath the MVC has a V_s of ~ 4.4 km/s, which is visibly low within the study area at 50 km deep.

Fig. 9 shows three depth profiles, AA', BB', and CC' along the northwest-southeast (NW-SE), northeast-southwest (NE-SW), north-northeast-south-southwest (NNE-SSW) directions, respectively (see Fig. 8i). The left three panels (Figs. 9a–c) show details of the sedimentary structure and upper-middle crust in the depth range of 0–20 km, and the right three panels (Figs. 9d–f) show crust and mantle structure from the surface to 50 km deep. Along the NW-SE AA' line, the sedimentary column thickens from south of the OFTB front towards the coast (right), except beneath the Sabine Uplift in the middle of the plain (Fig. 9a). The Moho starts at ~ 43 km deep beneath the SOA, shallowing slightly to the OFTB, and gradually decreases to ~ 23 km beneath the Gulf Coast Basin at the coast except for the Sabine Uplift, which has a slightly deeper Moho (Fig. 9d).

BB' runs from the east edge of the MVC to the easternmost coast of Texas. As expected, we observe a rapid increase of sediment thickness from the MVC to the coast, and a large low velocity anomaly in the uppermost crust beneath the southern ME (Fig. 9b). The crust beneath the MVC is ~ 36 km thick, thins rapidly to ~ 28 km beneath the southern ME, and thins gradually towards the coast (Fig. 9e).

Profile CC', in an NNE-SSW direction, extends from the eastern edge of the MVC to the coast of Louisiana and samples the western Black Warrior Basin and the Mississippi Salt Dome Basin. While the amount of sediment infill increases sharply from the OFTB to the coast (Fig. 9c), Moho depth decreases only slightly, from 35 to 30 km along the profile.

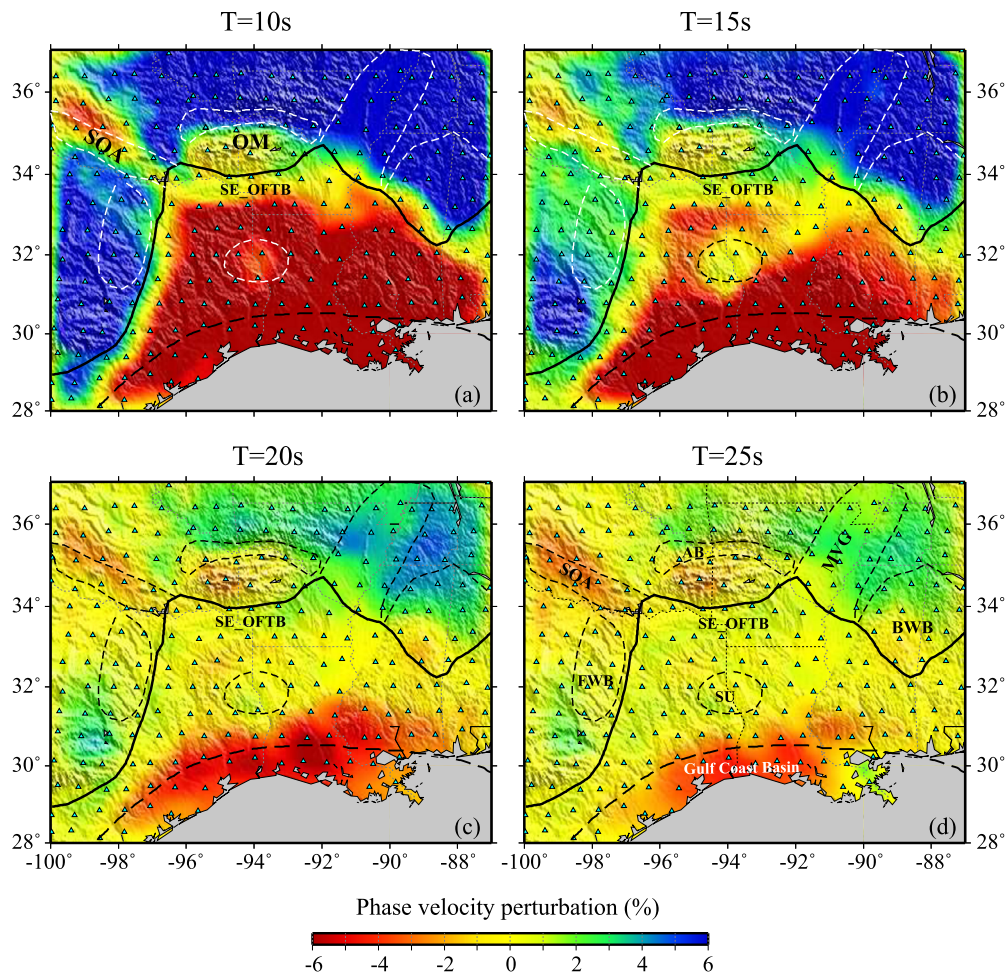


Fig. 7. Same as Fig. 7, except for phase velocities.

4. Discussion

The posterior density functions of the inverted Vs at each station suggest that these models are well constrained. We also compute the average phase velocity and Z/H ratio residuals (Figure S3) across the study area. The combined phase velocity residuals are generally less than 0.075 km/s (Figure S3a), and Z/H ratios are mostly in the range of 0.00–0.050 (Figure S3b). In general, our 3-D Vs model agrees with the model of Shen and Ritzwoller (2016) (hereinafter referred to as S&R16), but also shows some dissimilarity due to differences in data selection and inversion strategy. Figures S4 and S5 show the crustal thickness and S-wave velocity depth slices from the two models. In general, our model shows a better correlation between crustal thickness and the OFTB than S&R16 (Figure S4). Our model has a thinner crust beneath SOA in the northwest and Arkoma Basin and a thicker crust beneath the Mississippi Salt Dome Basin in the southeast (Figure S4c). Large differences in S-wave velocity are mainly present in the lowermost crust and uppermost mantle between the two models, which can largely be attributed to differences in Moho depth. Both models reveal a low-velocity anomaly within the entire crust beneath the SOA, which is spatially consistent with the low velocity anomaly in the upper mantle imaged by the P-wave traveltime tomography of Evanzia et al. (2014). In Figures S6, we further show a comparison of Moho depth estimates of our model, S&R16, and two active source models (Keller et al., 1989; Von Avendonk et al., 2015) along a NS profile at 94°W.

Direction of continental extension: Rifting between the Yucatan and North America is thought to have initiated in the late Triassic (ca. 201 Ma) in a NW-SE direction (e.g., Marton and Buffler, 1994; Pindell and Kennan, 2009). The rifting direction changed to NNE-SSW at ~166–150 Ma when seafloor spreading started, leading to the formation of the present-day deep-water GOM (e.g., Marton and Buffler, 1994; Pindell and Kennan, 2009). While the pole of rotation of seafloor spreading in the Florida Strait is constrained by a continent-ocean transform fault in eastern Mexico (e.g., Nguyen and Mann, 2016), the direction of continental rifting is unconstrained by seafloor data. We note that Moho depth underneath the GCP decreases significantly towards the coast in the SE direction (AA' line, Figs. 8i and 9d) but remains almost unchanged in the SSW direction (CC' line, Figs. 8i and 9f) inconsistent with NNE-SSW extension. The gradient of the Moho map between the OFTB boundary and coast in the area west to 94°W shows that the gradient overall lies in a dominant direction of ~N40°W (Figure S7). This suggests that original extension of the onshore crust was more nearly in a NW-SE direction.

Style of rifting: Based on the asymmetrical distribution of crustal structure and sedimentary records between the northern and southern parts of the GOM, Marton and Buffler (1993) argued that the geometry and internal deformation of the basin's conjugate passive margins are best explained by a rifting mode involving lithospheric simple shear rather than pure shear. In pure-shear rifting, extension occurs uniformly throughout the whole crust column, while in a simple-shear rifting deformation is concentrated

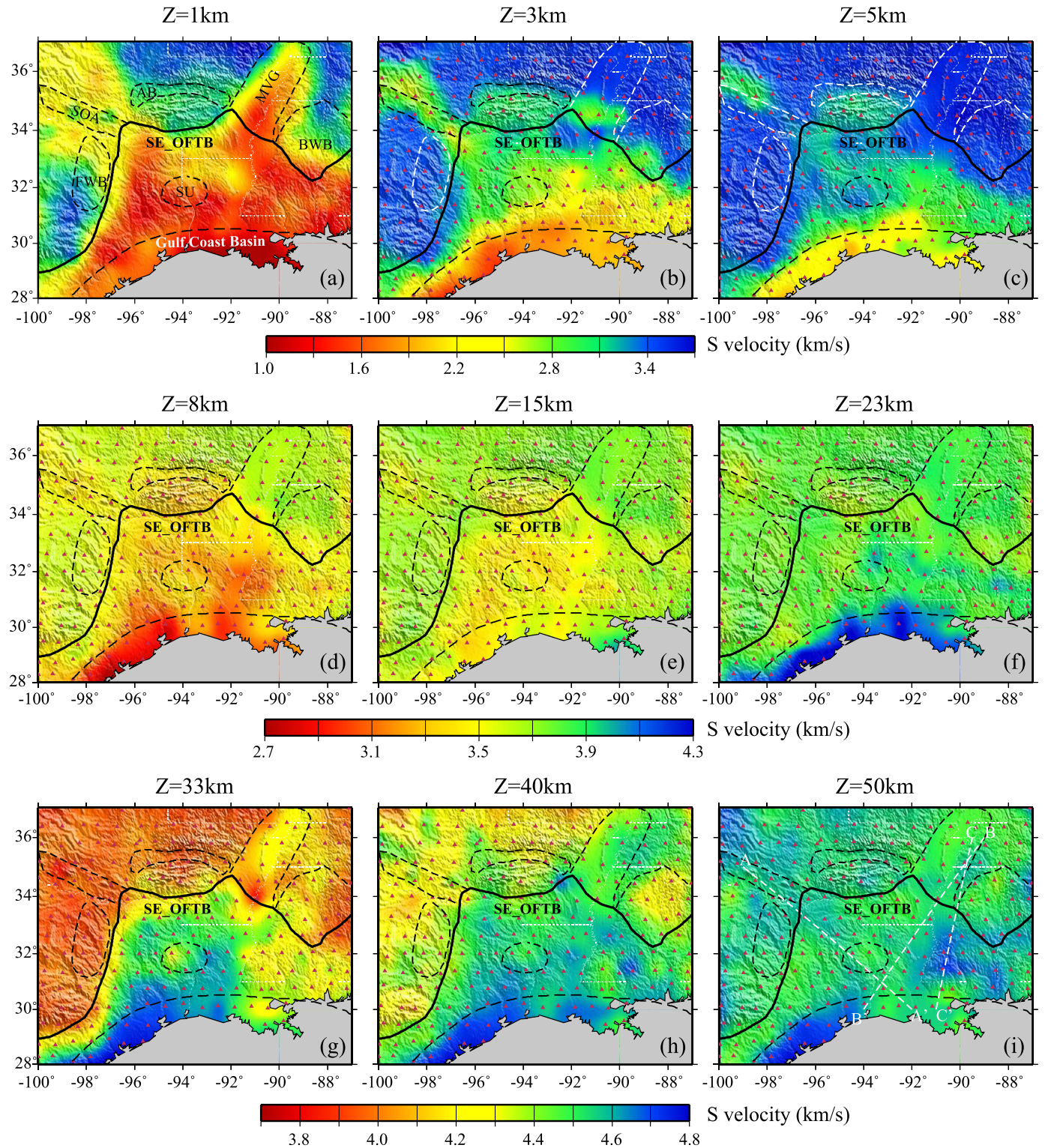


Fig. 8. Inverted 3-D S wave model plotted at various depths: 1 km (a), 3 km (b), 5 km (c), 8 km (d), 15 km (e), 23 km (f), 33 km (g), 40 km (h), and 50 km (i). Boundaries and tectonic units are similar to Fig. 1a. Solid black triangles are stations where 1-D Vs models are inverted. Note at 1 km (a), the GCP and MVC are featured by very low S-wave velocity, indicating the presence of unconsolidated sediments. The low Vs beneath the GCP extends to 8 km in large areas including the GCB. At middle crustal depth of 15 km (e), the Vs inside the GCP is still lower than its surroundings. At 23 km (f) the GCB enters into the mantle, and therefore appears as a high velocity anomaly, which is also seen at 33 km (g), 40 km (h) and 50 km (i). The uppermost mantle beneath the Mississippi Salt Dome Basin is also seen as a high Vs.

above a detachment fault. Interpretations of the GUMBO active seismic profiles in the offshore suggest that the stretched crystalline crust north of the GOM oceanic crust was intruded by rift related mafic melts to varying degrees from west to east (Christeson et al., 2014; Eddy et al., 2014; Van Avendonk et al., 2015).

We found that the GCP has uniformly high whole crustal V_p/V_s ratios, >1.8 , in the Gulf Coast Basin, i.e., within 100–200 km of the coast (Fig. 5b). This is consistent with a crustal column composed of thick, high V_p/V_s sediments and a high mafic content in the crystalline crustal supporting the model that the Gulf Coast was a

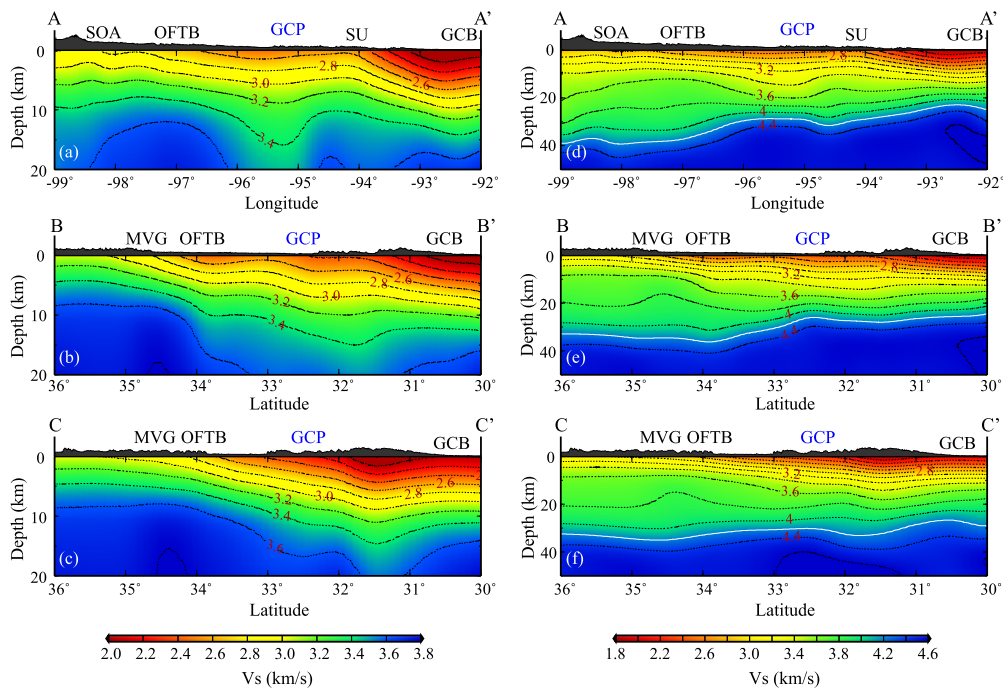


Fig. 9. Three cross-sections of the inverted 3-D S wave model, AA', BB', and CC' along the NW-SE, NE-SW, NNE-SSW directions are plotted in the depth range of 0–20 km (left three panels), and 0–50 km (right three panels), respectively. The geographic locations of the cross sections are delineated in Fig. 8i. The white lines in the right panels indicate the Moho. Different vertical exaggerations are employed in plotting the left and right panels. Note the systematic and different variations in sedimentary structures in (a), (b), (c) and Moho depth in (d), (e), and (f).

magmatic rift margin. Therefore, the observed high V_p/V_s ratio of the Gulf Coast Basin is consistent with a magmatic simple shear rifting model proposed by Marton and Buffler (1993).

Houston magnetic anomaly: Our model shows a high-velocity anomaly along the coast of southeast Texas at lower crust and uppermost mantle depths. The mantle velocities are similar to highly depleted cratonic lithospheric mantle with a high degree of melt extraction (Lee, 2003), suggesting a source for the crustal high velocities. Since a similar high-velocity anomaly is also observed in the 3-D V_s model of Shen and Ritzwoller (2016), we consider this a robust feature of the model, although we note that the anomaly is located at the edge of our study area, and thus is relatively poorly resolved (Figure S2). As mentioned above, this high-velocity anomaly correlates well with the Houston magnetic anomaly, argued by Mickus et al. (2009) to be caused by a buried volcanic rifted margin, although our observations place the top of this anomaly deeper in the crust than modeled by Mickus et al. (2009), at 20+ km vs 12–15 km. We note that Moho depth beneath the GOM continental shelf along GUMBO 1 is approximately the same as our modeled Moho at the coast (28–29 km), and that GUMBO 1 is interpreted as having been intruded by mafic melts (Van Avendonk et al., 2015). The GUMBO 1 seismic refraction model also reveals anomalously high-velocity structures in the lowermost crust and the uppermost mantle at various locations beneath the extended Texas continental margin and shows that the continent-ocean boundary occurs ~250 kilometers offshore. Both GUMBO 1 and coincident seismic reflection data lack evidence of seaward dipping reflectors this far west along the coast (Van Avendonk et al., 2015). We suggest that during the NW-SE continental rifting, the lower crust at least as far as north as the Texas Coast was intruded by mafic melts. When the local rifting direction changed to NNE-SSW as seafloor spreading commenced, magmatic activity shifted southward to the spreading ridge to accommodate changes in the stress field related to the new rifting direction. Our results appear consistent with a magmatic rift mar-

gin that involved magmatism as far north as the southeast coast of Texas.

Mississippi embayment: The ME separates the EW trending Ouachita range from the Appalachian range that runs roughly in the NS direction along the Atlantic coast of the US. The subsidence of the ME occurred in the late Cretaceous and early Tertiary, ~50–60 million years after cessation of GOM seafloor spreading at ~145 Ma (Burke, 1988). The origin of the embayment, originally attributed to the opening of GOM (e.g., Braile et al., 1986), is now thought to be caused by North America passing over the Bermuda hotspot during the late Cretaceous (Cox and Arsdale, 2002). Thermal uplift of the crust of the MVG and Reelfoot Rift was 1–3 km. The uplifted crust eroded, then subsided as North America moved west, resulting in a topographic low that filled to become the current ME sedimentary basin. Our model shows that the MVG is underlain by a high V_s layer at the bottom of the crust (Fig. 9g), plausibly indicating magmatic additions during the passage of the Bermuda plume. However, since the crust beneath MVG is slightly thin (~36 km) and has an average V_p/V_s ratio of 1.8, we argue that magmatic additions to the crust and underplating were minor.

We also found that V_s of the uppermost mantle beneath the MVG is slightly low, consistent with moderately high surface heat flow, 60–80 mW/m² (Blackwell and Steele, 1992). This suggests that the thermal residual of the Bermuda plume head is still seismically detectable (Campbell and Davies, 2006). The low velocity lithospheric mantle might also explain the presence of the New Madrid seismic zone, as it implies a zone of lithospheric weakness. In general, the observed seismic structures beneath the MVG are consistent with the scenario of a Bermuda hotspot origin for the ME.

5. Conclusions

In this study, we developed a 3-D model of the crust and upper mantle of the Gulf Coast and south-central US, with data

from 215 USArray stations. We used H- κ analysis of RFs to calculate a starting model, and then a joint inversion of Rayleigh wave phase velocities, Rayleigh wave ellipticity, and teleseismic P-coda waveforms to develop the final model. The model shows very strong spatial correlation between surface tectonic units and velocity structure: sedimentary column and crustal thickness, V_p/V_s ratio, and V_s . The OFTB front marks a velocity as well as topographic boundary that extends to the Moho, which is elevated by 5–10 km beneath the GCP relative to the adjacent terranes. The broad distribution of crustal thinning and high V_p/V_s ratio across the GCP are consistent with a simple-shear crustal rifting style. Crustal thinning towards the coast is more obvious in the SE direction, which confirms the general view that continental rifting initiated in a NW-SE direction, and later shifted to the NNE-SSW direction as seafloor spreading started. We observe a high velocity anomaly in the lower crust and the uppermost mantle beneath the southeast Texas coast that is coincident with the Houston magnetic anomaly. The magnetic anomaly, the seismic velocity and offshore seismic data provide evidence for mafic igneous intrusive rocks, suggesting a magmatically active rift margin with magmatism extending at least as far north as the Texas coast. We found that the MVG is underlain by ~ 36 km thick crust with a high-velocity lower crust and a slightly low velocity upper mantle, consistent with the hypothesis that the ME originated from late Cretaceous passage of North America over the Bermuda hotspot.

CRediT authorship contribution statement

Wenpei Miao: Data curation, Methodology, Visualization, Writing – original draft. **Fenglin Niu:** Conceptualization, Funding acquisition, Supervision, Writing – review & editing. **Guoliang Li:** Methodology. **Alan Levander:** Writing – review & editing.

Declaration of competing interest

The authors declare that they have no known competing financial interests or personal relationships that could have appeared to influence the work reported in this paper.

Acknowledgements

We thank IRIS and EarthScope for providing the data used in this study, and Luan Nguyen for constructive comments on the manuscript. We also thank Dr. Robert Porritt and an anonymous reviewer for their constructive comments and suggestions, which significantly improved the quality of this paper. G.L. was supported by the National Natural Science Foundation of China (41630209), and W.M. was supported by Rice University.

Appendix A. Supplementary material

Supplementary material related to this article can be found online at <https://doi.org/10.1016/j.epsl.2021.117257>.

References

- Afonso, J.C., Fullea, J., Griffin, W.L., Yang, Y., Jones, A.G., Connolly, J.A.D., O'Reilly, S.Y., 2013. 3-D multiobservable probabilistic inversion for the compositional and thermal structure of the lithosphere and upper mantle. I: a priori petrological information and geophysical observables. *J. Geophys. Res., Solid Earth* 118 (5), 2586–2617.
- Agrawal, M., Pulliam, J., Sen, M.K., Gurrola, H., 2015. Lithospheric structure of the Texas-Gulf of Mexico passive margin from surface wave dispersion and migrated Ps receiver functions. *Geochem. Geophys. Geosyst.* 16 (7), 2221–2239.
- Ainsworth, R., Pulliam, J., Gurrola, H., Evanzia, D., 2014. Sp receiver function imaging of a passive margin: transect across Texas's Gulf Coastal Plain. *Earth Planet. Sci. Lett.* 402, 138–147.
- Bird, D.E., Burke, K., Hall, S.A., Casey, J.F., 2005. Gulf of Mexico tectonic history: hotspot tracks, crustal boundaries, and early salt distribution. *Am. Assoc. Pet. Geol. Bull.* 89 (3), 311–328.
- Blackwell, D.D., Steele, J.L., 1992. DNAG Geothermal Map of North America, Scale 1:5,000,000. Geological Society of America.
- Bodin, T., Yuan, H., Romanowicz, B., 2014. Inversion of receiver functions without deconvolution—application to the Indian craton. *Geophys. J. Int.* 196, 1025–1033.
- Braile, L.W., Hinze, W.J., Keller, G.R., Lidiak, E.G., Sexton, J.L., 1986. Tectonic development of the New Madrid rift complex, Mississippi Embayment, North America. *Tectonophysics* 131, 1–21.
- Budnik, R.T., 1986. Left-lateral intraplate deformation along the Ancestral Rocky Mountains: implications for late Paleozoic plate motions. *Tectonophysics* 132, 195–214.
- Burke, K., 1988. Tectonic evolution of the Caribbean. *Annu. Rev. Earth Planet. Sci.* 16 (20), 201–230.
- Campbell, I.H., Davies, G.F., 2006. Do mantle plumes exist? *Episodes* 29, 162–168.
- Christeson, G.L., Van Avendonk, H.J.A., Norton, I.O., Snedden, J.W., Eddy, D.R., Karner, G.D., Johnson, C.A., 2014. Deep crustal structure in the eastern Gulf of Mexico. *J. Geophys. Res., Solid Earth* 119 (9), 6782–6801.
- Chong, J., Ni, S., Zhao, L., 2014. Joint inversion of crustal structure with the Rayleigh wave phase velocity dispersion and the ZH ratio. *Pure Appl. Geophys.* 172, 2585–2600.
- Clayton, R.W., Wiggins, R.A., 1976. Source shape estimation and deconvolution of teleseismic body waves. *Geophys. J. R. Astron. Soc.* 47, 151–177.
- Cox, R.T., Van Arsdale, R.B., 2002. The Mississippi embayment, North America: a first order continental structure generated by the Cretaceous superplume mantle event. *J. Geodyn.* 34, 163–176.
- Dunbar, J.A., Sawyer, D.S., 1987. Implications of continental crust extension for plate reconstruction: an example from the Gulf of Mexico. *Tectonics* 6, 739–755.
- Dziewonski, A.M., Bloch, S., Landisman, M., 1969. A technique for the analysis of transient seismic signals. *Bull. Seismol. Soc. Am.* 59, 427–444.
- Dziewonski, A.M., Anderson, D.L., 1981. Preliminary reference Earth model. *Phys. Earth Planet. Inter.* 25 (4), 297–356.
- Eddy, D.R., Van Avendonk, H.J.A., Christeson, G.L., Norton, I.O., Karner, G.D., Johnson, C.A., Snedden, J.W., 2014. Deep crustal structure of the northeastern Gulf of Mexico: implications for rift evolution and seafloor spreading. *J. Geophys. Res., Solid Earth* 119 (9), 6802–6822.
- Evanzia, D., Pulliam, J., Ainsworth, R., Gurrola, H., Pratt, K., 2014. Seismic Vp & Vs tomography of Texas & Oklahoma with a focus on the Gulf Coast margin. *Earth Planet. Sci. Lett.* 402, 148–156.
- Grand, S.P., 1994. Mantle shear structure beneath the Americas and surrounding oceans. *J. Geophys. Res., Solid Earth* 99, 11591–11621.
- Hall, S.A., Najmuddin, I.J., 1994. Constraints on the tectonic development of the eastern Gulf of Mexico provided by magnetic anomaly data. *J. Geophys. Res., Solid Earth* 99, 7161–7175.
- Harry, D.L., Londono, J., 2004. Structure and evolution of the central Gulf of Mexico continental margin and coastal plain, southeast United States. *Geol. Soc. Am. Bull.* 116 (1–2), 188–199.
- Haskell, N.A., 1962. Crustal reflection of plane P and SV waves. *J. Geophys. Res., Solid Earth* 67, 4751–4767.
- Herrin, E., Goforth, T., 1977. Phase-matched filters: application to the study of Rayleigh waves. *Bull. Seismol. Soc. Am.* 67 (5), 1259–1275.
- Herrmann, R.B., Ammon, C.J., 2004. Surface waves, receiver functions and crustal structure, in computer programs in seismology, version 3.30. http://www.eas.slu.edu/eqc/eqc_cps/CPS/CPS330/cps330c.pdf.
- Hildenbrand, T.G., 1985. Rift structure of the Northern Mississippi embayment from the analysis of gravity and magnetic data. *J. Geophys. Res., Solid Earth* 90, 12607–12622.
- Hudec, M.R., Norton, I.O., Jackson, M.P.A., Peel, F.J., 2013. Jurassic evolution of the Gulf of Mexico salt basin. *Am. Assoc. Pet. Geol. Bull.* 97 (10), 1683–1710.
- Keller, G.R., Braile, L.W., McMechan, G.A., Thomas, W.A., Harder, S.H., Chang, W.-F., Jardine, W.G., 1989. Paleozoic continent-ocean transition in the Ouachita Mountains imaged from PASSCAL wide-angle seismic reflection-refraction data. *Geology* 17, 119–122.
- Lee, C.-T.A., 2003. Compositional variation of density and seismic velocities in natural peridotites at STP conditions: implications for seismic imaging of compositional heterogeneities in the upper mantle. *J. Geophys. Res., Solid Earth* 108, 2441.
- Li, G., Chen, H., Niu, F., Guo, Z., Yang, Y., Xie, J., 2016. Measurement of Rayleigh wave ellipticity and its application to the joint inversion of high-resolution S wave velocity structure beneath northeast China. *J. Geophys. Res., Solid Earth* 121 (2), 864–880.
- Li, G., Niu, F., Yang, Y., Xie, J., 2018. An investigation of time-frequency domain phase weighted stacking and its application to phase velocity extraction from ambient noise's empirical Green functions. *Geophys. J. Int.* 212 (2), 1143–1156.
- Li, G., Niu, F., Yang, Y., Tao, K., 2019. Joint inversion of surface wave phase velocity, particle motion and teleseismic body wave data for sedimentary structures. *Geophys. Res. Lett.* 46 (12), 6469–6478.
- Lin, F.-C., Schmandt, B., Tsai, V.C., 2012. Joint inversion of Rayleigh wave phase velocity and ellipticity using USArray: constraining velocity and density structure

- in the upper crust. *Geophys. Res. Lett.* 39 (12), L12303. <https://doi.org/10.1029/2012GL052196>.
- Lin, F.-C., Tsai, V.C., Schmandt, B., 2014. 3-D crustal structure of the western United States: application of Rayleigh-wave ellipticity extracted from noise cross-correlations. *Geophys. J. Int.* 198 (2), 656–670. <https://doi.org/10.1093/gji/ggu160>.
- Marton, G., Buffler, R.T., 1993. Application of simple-shear model to the evolution of passive continental margins of the Gulf of Mexico basin. *Geology* 21, 495–498.
- Marton, G., Buffler, R.T., 1994. Jurassic reconstruction of the Gulf of Mexico basin. *Int. Geol. Rev.* 36, 545–586. <https://doi.org/10.1080/00206819409465475>.
- Meltzer, A., Rudnick, R., Zeitler, P., Levander, A., Humphreys, E., Karlstrom, K., Ekstrom, E., Carlson, C., Dixon, T., Gurnis, M., Shearer, P., Hilst, R.D., 1999. USArray initiative. *GSA Today* 9.
- Mickus, K.L., Stern, R.J., Keller, G.R., Anthony, E.Y., 2009. Potential field evidence for a volcanic rifted margin along the Texas Gulf Coast. *Geology* 37, 387–390. <https://doi.org/10.1130/G25465A.1>.
- Nguyen, L.C., Mann, P., 2016. Gravity and magnetic constraints on the Jurassic opening of the oceanic Gulf of Mexico and the location and tectonic history of the Western main transform fault along the eastern continental margin of Mexico. *Interpret.* 4 (1), SC23–SC33. <https://doi.org/10.1190/INT-2015-0110.1>.
- Niu, F., Bravo, T., Pavlis, G., Vernon, F., Rendon, H., Bezada, M., Levander, A., 2007. Receiver function study of the crustal structure of the southeastern Caribbean plate boundary and Venezuela. *J. Geophys. Res.* 112, B11308. <https://doi.org/10.1029/2006JB004802>.
- Pindell, J.L., Dewey, J.F., 1982. Permo–Triassic reconstruction of western Pangea and the evolution of the Gulf of Mexico/Caribbean region. *Tectonics* 1, 179–211.
- Pindell, J.L., Kennan, L., 2009. Tectonic evolution of the Gulf of Mexico, Caribbean and northern South America in the mantle reference frame: an update. *Geol. Soc. (Lond.) Spec. Publ.* 328 (1), 1–55.
- Shen, W., Ritzwoller, M.H., 2016. Crustal and uppermost mantle structure beneath the United States. *J. Geophys. Res., Solid Earth* 121 (6), 4306–4342. <https://doi.org/10.1002/2016JB012887>.
- Stern, J.R., Dickinson, W.R., 2010. The Gulf of Mexico is a Jurassic backarc basin. *Geosphere* 6, 739–754. <https://doi.org/10.1130/GES00585.1>.
- Stern, J.R., Anthony, E.Y., Ren, M., Lock, B.E., Norton, I., Kimura, J., Miyazaki, T., Hanyu, T., Chang, Q., Hirahara, Y., 2011. Southern Louisiana salt dome xenoliths: first glimpse of Jurassic (ca. 160 Ma) Gulf of Mexico crust. *Geology* 39 (4), 315–318.
- Tanimoto, T., Rivera, L., 2008. The ZH ratio method for long-period seismic data: sensitivity kernels and observational techniques. *Geophys. J. Int.* 172 (1), 187–198. <https://doi.org/10.1111/j.1365-246X.2007.03609.x>.
- Van Avendonk, H.J.A., Christeson, G.L., Norton, I.O., Eddy, D.R., 2015. Continental rifting and sediment infill in the northwestern Gulf of Mexico. *Geology* 43 (7), 631–634. <https://doi.org/10.1130/G36798.1>.
- Yao, Y., Li, A., 2016. Lithospheric velocity model of Texas and implications for the Ouachita orogeny and the opening of the Gulf of Mexico. *Geophys. Res. Lett.* 43 (23), 12046–12053. <https://doi.org/10.1002/2016GL071167>.